Case Studies in Thermal Engineering 64 (2024) 105436

Contents lists available at ScienceDirect

Case Studies in Thermal Engineering

journal homepage: www.elsevier.com/locate/csite

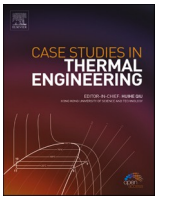

CFD numerical simulation, verification with experimental results and internal flow analysis of bristle turbines

Sun Sheng Yang [a], Dong Ya Li [a], David Kupka [b], Jan Kolonicny [b], Punit Singh [c,*]

[a] National Research Center of Fluid Machinery Engineering and Technology, Jiangsu University, Zhenjiang, Jiangsu, 212013, China
[b] Energy Research Centre, CEET, VSB – Technical University of Ostrava, 17. listopadu 2172/15, 708 00, Ostrava, Poruba, Czech Republic
[c] Centre for Sustainable Technologies, Indian Institute of Science, CV Raman Road, Bangalore, 560012, India

ARTICLE INFO

Handling Editor: Huihe Qiu

Keywords:
Bristle turbine
Bladeless rotor
Waste heat recovery
CFD simulation
Internal flow analysis

ABSTRACT

In industrial facilities, a considerable amount of waste heat is often generated. However, due to the high costs associated with traditional methods of recovery, which do not align with the economic interests of enterprises, this waste heat is frequently wasted. With technological advancements, the bristle turbine has been proposed as a solution capable of effectively managing waste gases and providing added value to enterprises. Its advantages lie in its simple structure, easy installation, low rotational speed, and high reliability, offering a new option for waste heat recovery and utilization. Despite its potential, no previous research has conducted a detailed simulation of the bristle turbine, particularly focusing on internal flow dynamics, energy loss mechanisms, drag forces, and entropy generation. This study is the first to explore these critical aspects, making a novel contribution to the field. The paper presents the computational fluid dynamics (CFD) simulation of a 20 kW bristle turbine. The numerical simulation results are in good agreement with experimental results. Subsequently, the isentropic efficiency of the turbine at different speeds is simulated, and the performance of the turbine under off-design conditions is analyzed. By investigating the energy loss mechanisms within the turbine, optimization designs are proposed.

1. Introduction

In recent years, due to the increasing demand for energy efficiency and sustainable development, the recovery of low-grade waste heat has become an important focus area. To effectively recover and utilize low-grade waste heat in industrial production, various technologies and methods have been developed to reduce environmental impact and promote sustainability across different industrial and commercial sectors [1]. Su et al. [2] categorized multiple typical waste heat generating industries into three classes based on the grade of waste heat, providing a comprehensive review of the potential and methods of waste heat recovery.

Industries such as pulp and paper manufacturing, food processing, and textiles often generate high-pressure steam, which is typically reduced to a safe range using pressure reducing valves to ensure that the system pressure does not exceed the set value, thereby ensuring the normal operation of the steam system [3]. The use of pressure reducing valves does not effectively utilize high-pressure steam, adversely affecting the economic benefits of enterprises [4].

The use of an appropriate pressure reduction device instead of pressure reducing valves is particularly important. Therefore, the

* Corresponding author.
E-mail address: punitsingh@iisc.ac.in (P. Singh).

https://doi.org/10.1016/j.csite.2024.105436
Received 18 September 2024; Received in revised form 28 October 2024; Accepted 4 November 2024
Available online 6 November 2024

turbine expander is a good choice, as it can achieve pressure reduction and provide power output [5]. By converting the pressure energy of steam into kinetic energy through the principle of steam converting the rotor's kinetic energy into mechanical energy, steam pressure can be reduced. Energy is then extracted from the fluid by the rotation of turbine blades and converted into power output. For example, Peng et al. [6] designed a 1.5 kW single-stage partial admission impulse turbine for waste heat recovery from an internal combustion engine and conducted 3D CFD simulations, achieving a total-to-static efficiency of 42.5 %. Additionally, experimental research was carried out on a two-stage counter-rotating partial admission turbine. The results demonstrated that adding a second stage effectively recovers the energy from the first rotor's outlet, significantly improving overall performance [7,8]. These findings mark important progress in the development of kW-class steam turbines.

With technological advancements, the concept of a miniaturized bladeless turbine has been proposed for waste heat applications or as an alternative to pressure reducing valves in steam pipeline systems with different pressure levels. Kupka et al. [9] designed and manufactured a micro-scale bladeless-type steam turbine with an output power of approximately 20 kW (also called bristle turbine because its rotating parts are similar to bristle), conducted experimental tests, and analyzed the isentropic efficiency of the turbine under different mass flow conditions. Compared to traditional turbines, this unconventional turbine has a simple structure, low-cost operation and maintenance, and high flexibility since it can be quickly started and stopped, which are factors/properties that strongly influence applicability in practice, particularly in the sub-MW class.

At present, with the exception of a Tesla turbine, there is a lack of literature on the numerical simulation of micro-scale bladeless-type steam turbine, and, to the authors' knowledge, only one study has conducted experimental tests on them [9]. However, there has been no detailed numerical simulation of the internal flow of the turbine. Due to the limitations of experimental methods, it is difficult to fully understand the internal flow mechanism and performance characteristics of miniaturized bladeless turbines based solely on experimental results. Therefore, it is essential to conduct a detailed examination of the internal flow field of miniaturized bladeless turbines through CFD numerical simulation. Similar to other unconventional turbines such as jet propulsion turbines [10], tangential turbines with rotating channels [11], or Tesla turbines [12], they all feature unconventional bladeless forms, with the latter two being impulse turbines, where most of the expansion occurs within the nozzle. Regardless of their operating principles, the nozzle is a key component capable of greatly influencing the overall performance of bladeless turbines. Since the nozzle is one of the main contributors to efficiency loss (along with nozzle-rotor interaction), special concern must be paid to its proper design to make these turbines more feasible.

Among unconventional bladeless turbines, the Tesla turbine is frequently investigated with a focus on its application at the microscale level, and scholars have conducted quite a lot of numerical simulations and experimental research on it. Siddiqui et al. [13] conducted a CFD analysis of a Tesla bladeless turbine using compressed air as the working fluid, analyzing various flow states using laminar and turbulent characteristics, and evaluating the turbine's power coefficient and efficiency. Recent research by Akele et al. [14] has focused on the design, construction, and simulation of Tesla turbines and pumps, emphasizing the importance of numerical simulation in understanding the performance of these systems. Ciappi et al. [15] through the validation of a commercial 3D CFD model, confirmed the effectiveness of the two-dimensional EES model and demonstrated the reliability of the analysis method in Tesla turbine design, filling a gap in the literature. Schosser et al. [16] summarized the numerical simulation of incompressible laminar flow in bladeless radial turbines, revealing the accuracy of simplified analytical performance predictions and flow field given a specific geometric shape, providing important guidance for numerical calculations.

Manfrida et al. [17] studied the optimal geometric shape of Tesla turbine rotors used in the micro power generation field, finding that the gap between disks and the outlet diameter largely determines the power generation capability. In addition, Hamdani et al. [18] further analyzed the relationship between disk gaps, number of disks, disk diameter, and torque.

However, experimental data and CFD numerical simulation studies on other types of bladeless turbines are very scarce. Only one prototype of a jet propulsion steam turbine has been built and tested, studying the relationship between a pressure ratio and isentropic efficiency, and analyzing the reasons for efficiency reduction with increasing pressure. The results indicate the need for better designs to improve efficiency, such as using different combinations of labyrinth seal designs and more efficient nozzles [10]. Benini et al. [19] provided a detailed introduction to this type of jet propulsion turbine, including its design, manufacturing, and operation stages. Barbarelli et al. [20] studied a tangential flow turbine with rotating channels, which is suitable for regions of low specific speed (Ns) and high specific diameter (Ds), overcoming the performance disadvantages of traditional turbines in this range. Based on the work of Scornaienchi et al. [21], Barbarelli et al. [22] optimized a small tangential flow turbine with rotating channels and tangential inlet nozzles, and developed a prototype with five guide vanes, achieving a maximum efficiency of 43.5 % and a maximum power of 11.2 kW.

However, to the best of our knowledge, detailed aerodynamic analysis of bristle turbines has not been previously reported. This paper addresses this critical research gap by conducting a numerical analysis on a single-stage 20 kW bristle turbine, validating experimental results using three-dimensional computational fluid dynamics (CFD) simulations. By analyzing the internal flow characteristics within the bristle turbine, this study fills a significant gap in numerical simulation research, particularly regarding the interaction between internal flow and the bristles. These findings provide essential insights that can guide the optimization of design and performance in micro-scale bladeless turbines, contributing to future advancements in this area.

2. Objects and methods

2.1. Bristle turbine model

The bristle turbine analyzed in this paper is suitable for the recovery and utilization of low-grade waste heat in industrial

production, serving as an alternative to pressure reducing valves. High-pressure steam passes through the bristle turbine, reducing the pressure to a range acceptable for subsequent equipment. It mainly consists of a volute (containing an inlet chamber with nine CD nozzles), a rotor, and an outlet pipe, as shown in Fig. 1. The decision to use nine nozzles was based on comprehensive considerations of design, flow dynamics, and mechanics. Compared to the traditional circumferential uniform distribution, grouping the nozzles into a single block simplifies the mechanical design, manufacturing, and assembly processes. It also streamlines the fluid supply system, as steam can be supplied from a single inlet point, eliminating the need for a complex flow distribution network around the entire circumference. This centralized configuration reduces potential flow losses and allows for a more direct and controlled fluid delivery. The purpose of this paper is to analyze the internal flow characteristics of the bristle turbine through CFD simulation, elucidating the internal energy loss mechanism and filling the gap in the numerical analysis of this unconventional turbine. This provides a means for performance prediction and identification of key areas for aerodynamic optimization to enhance the overall performance of bristle turbines under design and off-design operating conditions.

2.2. CFD model

To reduce the computational domain grid size, Ansys ICEM was used to create a hexahedral grid for the rotor and outlet pipe. Ansys Meshing was employed to generate a tetrahedral grid for the volute.

The Ansys CFX solver was used for numerical computation, with the standard k-epsilon turbulence model. The simulation results are sensitive to the properties of the actual working fluid used in the system. In this study, the real gas dry steam equation was selected to describe the properties of the working fluid. Boundary conditions were set using inlet and outlet pressures. Total pressure was set at the inlet of the computational domain, while static pressure was set at the outlet. The rotor region was defined as a rotating domain with a speed of 9840 rpm, while the remaining regions were set as stationary domains. The rotor-stator interface with a pitch of 360° was set as a rotor-stator type interface, and interfaces between stationary domains were set as General Grid Interface (GGI). All walls were assigned no-slip conditions. The reference pressure was set to 0 Pa to obtain absolute pressure directly. The convergence criterion was set to reduce all scaled residuals below 1e-4. CFX simulation domain and grid are shown in Fig. 2.

To ensure the accuracy of the calculations, grid independence verification was conducted. In the entire bristle turbine, the nozzle and turbine rotor mesh play a crucial role in numerical simulation. Five sets of grids with different numbers of elements were generated, and calculations were performed under the same operating conditions. The isentropic efficiency of the turbine was used as the reference value for evaluation, as shown in Fig. 3. It can be seen that the number of grid elements begins to stabilize at 10 million, and higher mesh resolution has little impact on the solution accuracy, whereas required computational time is considerably increased. For considerations of computational efficiency, 10 million grid elements were used as the standard for CFD numerical simulation in the study.

3. Theory

3.1. Dimensionless number analysis

As an unconventional expansion component, it is essential to validate the dimensionless parameters of the bristle turbine. Balje [23] proposed different applicable ranges for expansion components based on the magnitude of a specific speed. Therefore, the rationality of the selection of expansion components can be judged based on the specific speed N_s and specific diameter D_s. The definitions of N_s and D_s are as follows:

$$N_s = \frac{\omega\sqrt{m/\rho_0}}{(\Delta h_{is})^{3/4}} \quad [-] \tag{1}$$

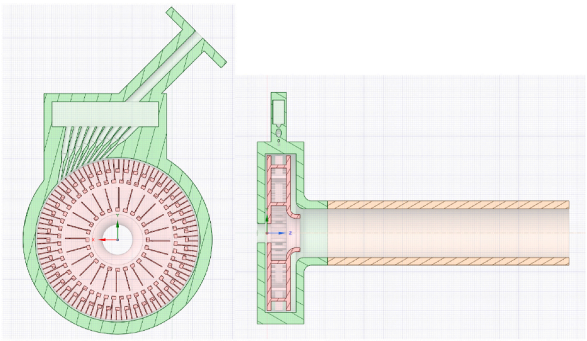

Fig. 1. Bristle turbine model.

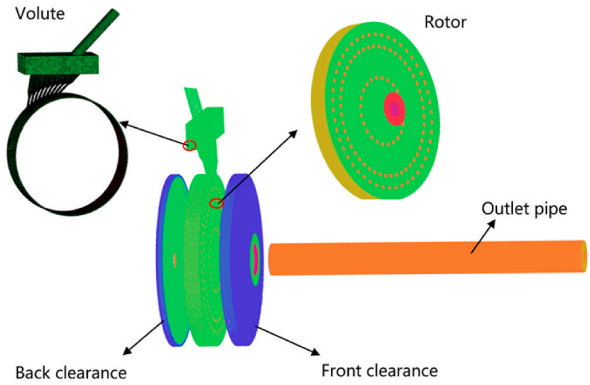

Fig. 2. Domain and mesh for CFX simulation.

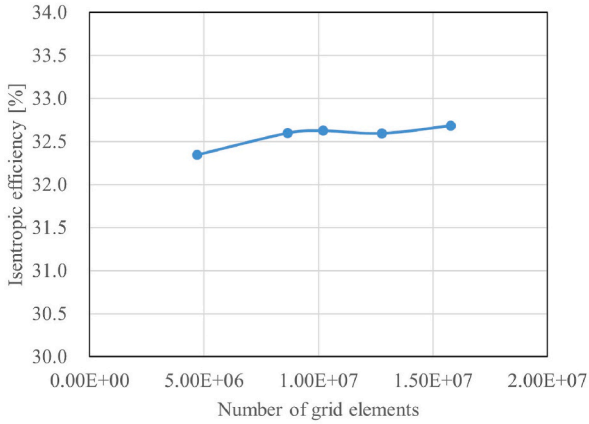

Fig. 3. Mesh sensitivity analysis.

$$D_s = \frac{D(\Delta h_{is})^{1/4}}{\sqrt{m/\rho_0}} \quad [-] \tag{2}$$

Where ω [rad·s^{-1}] is the angular velocity of the turbine rotation; m [kg·s^{-1}] is the mass flow rate; ρ_0 [kg·m^{-3}] is the density at the turbine inlet; Δh_{is} [kJ·kg^{-1}] is the isentropic enthalpy drop during the expansion process of the turbine; D [m] is the outer diameter of the turbine rotor.

The input parameters for conducting CFD analysis of the bristle turbine are shown in Table 1.

Based on the experimental results of Kupka et al. [9], a set of Ns and Ds data was obtained, and the data points were superimposed onto the Balje chart [23], as illustrated in Fig. 4. The figure shows that the experimental data points for the bristle turbine fall within a speed ratio range of 0.1–0.4, similar to the Terry turbine and matching with certain impulse turbines. Thereby validating the rationality of the selection of the expansion component.

Table 1
Bristle turbine input parameters.

Parameter	Value
Total pressure at the turbine inlet P_0 [MPa]	1
Total temperature at the turbine inlet T_0 [K]	463.15
Static pressure at the turbine outlet P_{out} [MPa]	0.1
Mass flow rate of steam m [kg·s^{-1}]	0.216
Density at the turbine inlet ρ_0 [kg·m^{-3}]	4.992
Turbine rotational speed n [rpm]	9840
Turbine diameter D [m]	0.4

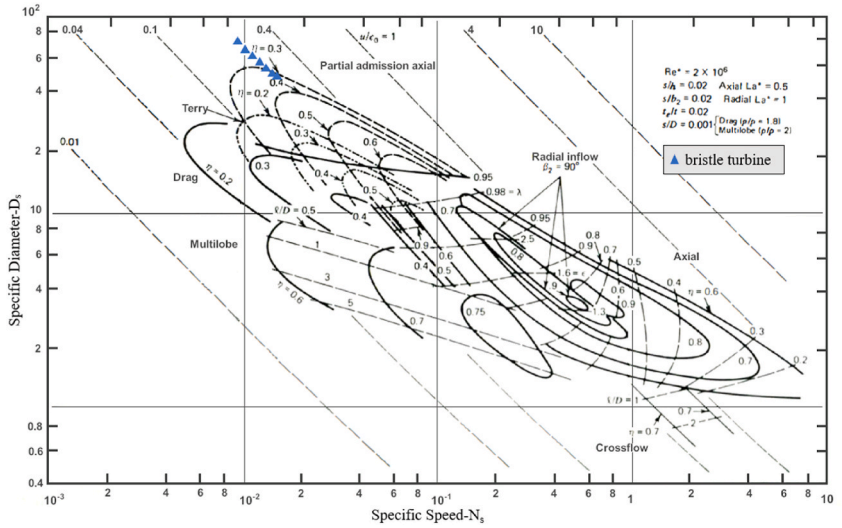

Fig. 4. Ns-Ds chart for bristle turbine (data points superimposed onto Ns-Ds mother chart taken from Ref. [23]).

3.2. Supersonic nozzle

The pressure drop of the bristle turbine mainly occurs at the nozzle, which means that the turbine belongs to the category of impulse type turbines. The design of the nozzle plays a crucial role in the overall performance of the bristle turbine due to high flow acceleration in the nozzle and associated irreversibility resulting in energy loss. In this study, it is assumed that the pressure ratio at the inlet and outlet of the turbine is equal to that of the nozzle, so the degree of reaction of the stage is zero. Therefore, the pressure at the outlet of the nozzle is the same as that at the outlet of the turbine. Due to the high expansion ratio of the turbine in this study, CD nozzles are used to avoid choked flow and overcome the limitations of convergent nozzles. This is because they can accommodate a larger range of expansion ratios to produce desired mass flow rate. The principle of the CD nozzle is depicted in Fig. 5, where sonic speed is achieved at the throat and supersonic speed is achieved in the expansion section.

Assuming that the flow in the nozzle is adiabatic, the throat cross-sectional area A_t can be expressed as

$$A_t = m \Big/ \sqrt{\frac{2\kappa}{\kappa-1} P_0 \rho_0 \left(PR_{cr}^{\frac{2}{\kappa}} - PR_{cr}^{\frac{\kappa+1}{\kappa}} \right)} \quad [\mathrm{m}^2] \tag{3}$$

where m [kg·s^{-1}] is the mass flow rate, κ [−] is the heat capacity ratio, P_0 [Pa] is the total inlet pressure, ρ_0 [kg·m^{-3}] is the inlet density, and PR_{cr} [−] is the critical pressure ratio which can be calculated from Eq. (4).

$$PR_{cr} = \left(\frac{2}{\kappa+1} \right)^{\frac{\kappa}{\kappa-1}} \quad [-] \tag{4}$$

The nozzle outlet cross-sectional area A_e [m^2] can be expressed as

$$\frac{A_e}{A_t} = PR_{cr} \sqrt{\frac{\kappa-1}{\kappa+1} \frac{1}{PR^{\frac{2}{\kappa}} - PR^{\frac{\kappa+1}{\kappa}}}} \quad [-] \tag{5}$$

The nozzle pressure ratio PR is defined as

$$PR = \frac{P_{out}}{P_0} \quad [-] \tag{6}$$

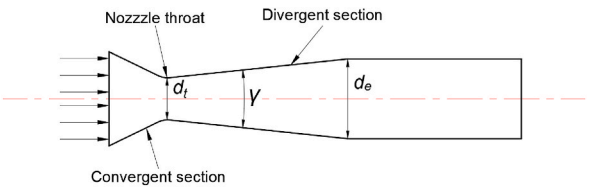

Fig. 5. Schematic of the CD nozzle.

And the specific heat ratio κ can be obtained from the following expression

$$\kappa = \frac{c_{pm}}{c_{pm} - R} \quad [-] \tag{7}$$

in which R [J·K^{-1}·mol^{-1}] is the gas constant and c_{pm} is the average specific heat capacity at constant pressure

$$c_{pm} = \frac{\Delta h_{is}}{T_0 - T_{out,is}} \quad \left[\mathrm{J \cdot kg^{-1} \cdot K^{-1}}\right] \tag{8}$$

Where Δh_{is} [J·kg^{-1}] is the ideal enthalpy drop of the nozzle, which can be obtained by REFPROP software [24]. In this paper, nine individual nozzles are used for research. The main geometric parameters of the nozzle are shown in Table 2.

3.3. Turbine rotor

The rotor consists of two concentric disks of the same diameter, with brush-like bristles fixed on the disks and arranged at equal intervals along the circumference, resembling bristles. Supersonic steam flow exiting the nozzle outlet impinges on the bristles of 1.6 mm diameter, converting kinetic energy into mechanical energy, thereby driving the turbine rotor to rotate and generate output work. The principle of impact in the bristle region is illustrated in Fig. 6. When steam impacts the bristles, part of its kinetic energy is converted into mechanical energy, while the remaining portion is converted into heat, resulting in a decrease in steam temperature.

The mechanical power transmitted from the turbine shaft can be obtained using Eq. (9).

$$P = \frac{n \bullet \tau}{9550} \quad [\mathrm{kW}] \tag{9}$$

Where τ [N·m] is the torque of the rotor and n [rpm] is rotational speed of the rotor.

The torque value is directly determined from the CFD post-processing results using the overall momentum of the turbine rotor.

3.4. Entropy production theory

Based on the second law of thermodynamics, there is always energy loss due to dissipative effects in mechanical processes. This process is irreversible and is always accompanied by an increase in entropy. The evaluation of irreversible losses in flow largely depends on the concept of entropy production rate (EPR). This concept, derived from the entropy transport equation, effectively quantifies the magnitude of local irreversible losses. The specific expression for the volumetric entropy production rate is provided in the literature [25]:

$$\dot{S}_{PRO,\overline{D}} = \frac{\mu}{\overline{T}}\left\{2\left[\left(\frac{\partial \overline{u}}{\partial x}\right)^2 + \left(\frac{\partial \overline{v}}{\partial y}\right)^2 + \left(\frac{\partial \overline{w}}{\partial z}\right)^2\right] + \left(\frac{\partial \overline{u}}{\partial y} + \frac{\partial \overline{v}}{\partial x}\right)^2 + \left(\frac{\partial \overline{u}}{\partial z} + \frac{\partial \overline{w}}{\partial x}\right)^2 + \left(\frac{\partial \overline{v}}{\partial z} + \frac{\partial \overline{w}}{\partial y}\right)^2\right\} \quad \left[\mathrm{W \cdot m^{-3} \cdot K^{-1}}\right] \tag{10}$$

$$\dot{S}_{PRO,D'} = \frac{\mu}{\overline{T}}\left\{2\left[\overline{\left(\frac{\partial u'}{\partial x}\right)^2} + \overline{\left(\frac{\partial v'}{\partial y}\right)^2} + \overline{\left(\frac{\partial w'}{\partial z}\right)^2}\right] + \overline{\left(\frac{\partial u'}{\partial y} + \frac{\partial v'}{\partial x}\right)^2} + \overline{\left(\frac{\partial u'}{\partial z} + \frac{\partial w'}{\partial x}\right)^2} + \overline{\left(\frac{\partial v'}{\partial z} + \frac{\partial w'}{\partial y}\right)^2}\right\} \left[\mathrm{W \cdot m^{-3} \cdot K^{-1}}\right] \tag{11}$$

Where, $\dot{S}_{PRO,\overline{D}}$ [W·m^{-3}·K^{-1}] represents the direct (viscous) dissipation entropy production rate caused by time-averaged movement, $\dot{S}_{PRO,D'}$ [W·m^{-3}·K^{-1}] represents the indirect (turbulent) dissipation entropy production rate caused by velocity fluctuations. $\overline{T}$ [K] represents the local mean temperature, μ [Pa·s] is the dynamic viscosity, $\overline{u}, \overline{v}, \overline{w}$ and u', v', w' [m·s^{-1}] are respectively the time-averaged and fluctuating velocities in the flow field in the direction of x, y, and z.

In the Reynolds-Averaged Navier-Stokes (RANS) method, the fluctuating velocity components are not included in the governing equations, leaving only the time-averaged components available for iterative solutions. Therefore, the CFD post-processing calculates the direct dissipation rather than the indirect dissipation. In conjunction with the k-ε turbulence model, the right-hand side of equation (11) can be replaced by the product of density ρ [kg·m^{-3}] and the turbulence dissipation rate ε [m^2·s^{-3}].

$$\dot{S}_{PRO,D'} = \frac{\rho \varepsilon}{\overline{T}} \quad \left[\mathrm{W \cdot m^{-3} \cdot K^{-1}}\right] \tag{12}$$

Additionally, high velocity gradients exist in the wall region, generating significant wall effects that result in entropy production.

Table 2
Bristle turbine nozzle geometric parameters.

Parameter	Value
Throat diameter d_t [mm]	4.65
Outlet diameter d_e [mm]	7.28
Angle of spread γ [°]	7
Number of nozzles	9

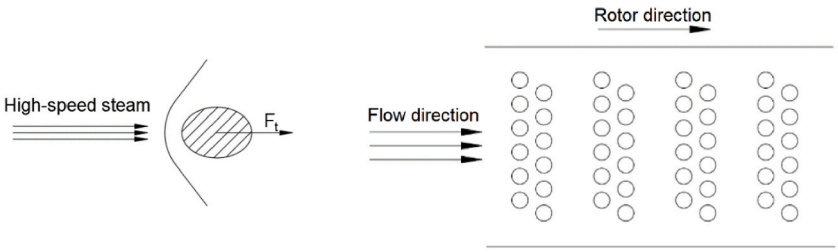

Fig. 6. Schematic diagram of steam flow impacting bristles (thrust elements).

Duan et al. [26] proposed a widely adaptable wall function with high computational accuracy to calculate the unit area entropy production rate near the wall, $\dot{S}_{PRO,W}$ [W·m^{-2}·K^{-1}].

$$\dot{S}_{PRO,W} = \frac{\vec{\tau}_w \bullet \vec{v}_w}{\overline{T}} \quad \left[\mathrm{W \cdot m^{-2} \cdot K^{-1}}\right] \tag{13}$$

Where, $\vec{\tau}_w$ [Pa] represents the wall shear stress, $\vec{v}_w$ [m·s^{-1}] represents the velocity at the center of the first layer of grid cells adjacent to the wall.

By integrating the dissipation entropy production rate and the wall entropy production rate over each computational domain, the losses within each component of the system can be determined. The detailed derivation of the corresponding formulas is shown below.

$$P_D = \int_V \overline{T} \cdot \left(\dot{S}_{PRO,\overline{D}} + \dot{S}_{PRO,D'}\right) dV \quad [\mathrm{W}] \tag{14}$$

$$P_W = \int_A \overline{T} \cdot \dot{S}_{PRO,W}\, dA \quad [\mathrm{W}] \tag{15}$$

In the equations, P_D and P_W [W] represent the entropy losses caused by dissipation and wall friction, respectively. These two components of entropy loss account for only a part of the total loss. There are other unaccounted entropy losses, such as those caused by heat conduction, and irreversible phase transitions. We categorize these unquantifiable entropy losses as P_{others} [W], to facilitate a comprehensive quantification of the total losses.

4. Results and discussions

4.1. With constant mass flow rate and varying speed

4.1.1. Verification of experimental results and CFD numerical simulation results

The reliability verification of CFD numerical simulation method is an important problem. This paper makes a comparison based on the experimental data tested by Kupka et al. [9]. The comparison of CFD simulation results and experimental results at design operating conditions is shown in Table 3.

From Tables 3, it can be observed that the relative difference between the CFD simulation results and experimental results for generator power is less than 10 %. Given that the CFD numerical simulations were conducted under adiabatic conditions, neglecting thermal losses at the walls, the calculated generator power is slightly higher. Therefore, the CFD numerical simulation method demonstrates a certain level of reliability.

Based on the original bristle turbine model, the non-design performance of the turbine was estimated using CFD simulation. Under a constant expansion ratio and mass flow rate conditions, the turbine's performance under off-design conditions was simulated by varying the rotational speed of the rotating domain. Starting from 9840 rpm, with increments of 1500 rpm, six data sets were obtained as shown in Fig. 7. In Fig. 7(a), the relationship between the velocity ratio and isentropic efficiency is presented. Although the design operating point is 9840 rpm, the highest efficiency point occurs not at the design condition, but near a blade tip speed ratio of 0.27 (approximately 11400 rpm). Fig. 7(b) displays the turbine's performance under different flow coefficients and stage loading coefficients. Compared to conventional turbines, the performance appears slightly inferior; however, the bristle turbine is a relatively

Table 3
CFD simulation results and experimental results.

Item	Steam mass flow rate [kg·h^{-1}]	Steam inlet pressure [MPa]	Steam inlet temperature[K]	Steam outlet pressure [MPa]	Generator power [kW]	Rotational speed [rpm]
experiment	777.0	1.076	463.65	0.1012	20.65	9681
numerical simulation	781.82	1.0	463.15	0.1045	22.87	9840

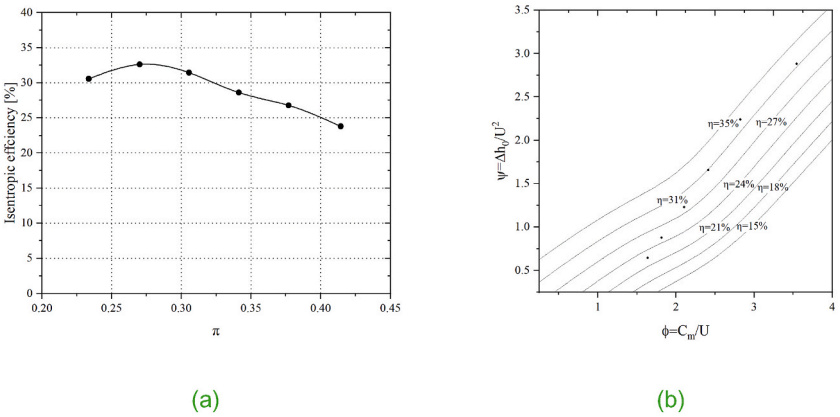

Fig. 7. Performance variations of the turbine under different operating conditions.

new and less-explored design with significant optimization potential yet to be realized.

The velocity ratio can be obtained using Eq. (16).

$$\pi = \frac{u}{c_0} \quad [-] \tag{16}$$

Where u [m·s^{-1}] is the circumferential linear velocity at the rotor inlet, and c_0 [m·s^{-1}] is the ideal expansion velocity:

$$c_0 = \sqrt{2(h_{01} - h_{2s})} \quad [\mathrm{m \cdot s^{-1}}] \tag{17}$$

Since kinetic energy at the turbine outlet is not utilized and is completely wasted, the isentropic efficiency in this paper is the total-to-static isentropic efficiency:

$$\eta = \frac{h_{01} - h_{02}}{h_{01} - h_{2s}} \quad [-] \tag{18}$$

Where h_{01} [J·kg^{-1}] is the stagnation enthalpy at the nozzle inlet, h_{02} [J·kg^{-1}] is the stagnation enthalpy at the turbine outlet, and h_{2s} [J·kg^{-1}] is the isentropic static enthalpy at the turbine outlet.

4.1.2. Analysis of internal flow

Detailed analysis of the internal flow of the bristle turbine has not been reported in the existing literature, leaving a gap in research. Conducting internal flow analysis is essential for optimizing and innovating the sustainability of the bristle turbine. To facilitate internal analysis, we created a symmetrical section of the nozzle, as shown in Fig. 8.

High-pressure and high-temperature steam passes through a supersonic nozzle, where thermal energy is converted into kinetic energy. At the nozzle outlet, the pressure decreases, and the flow velocity increases significantly. Subsequently, the high-speed steam enters the passages of the rotor. Within these passages, the high-speed steam impacts the bristle-like structures, generating a powerful thrust force that drives the turbine's rotation. The steam then passes through a nozzle structure similar to gradual contraction and expansion, experiencing secondary expansion, which further accelerates the steam. As the steam flows through the bristles, a phenomenon of diversion occurs, and the conversion of kinetic energy leads to a gradual decrease in velocity. Fig. 9 illustrates the velocity distribution of steam inside the turbine, with rotational speeds increasing from the design value of 9840 rpm (a) to (f) at intervals of

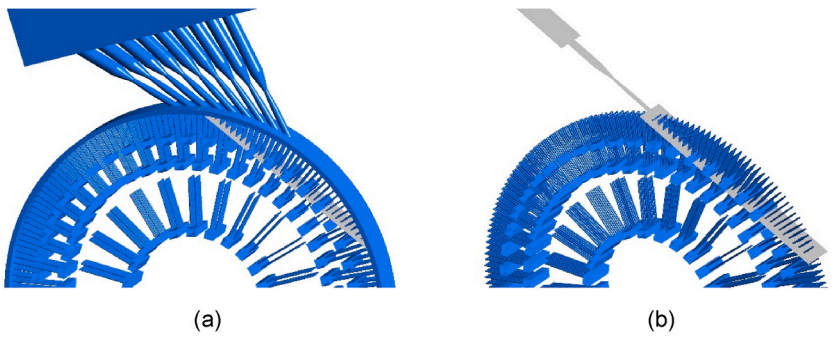

Fig. 8. Symmetrical profile of nozzle.

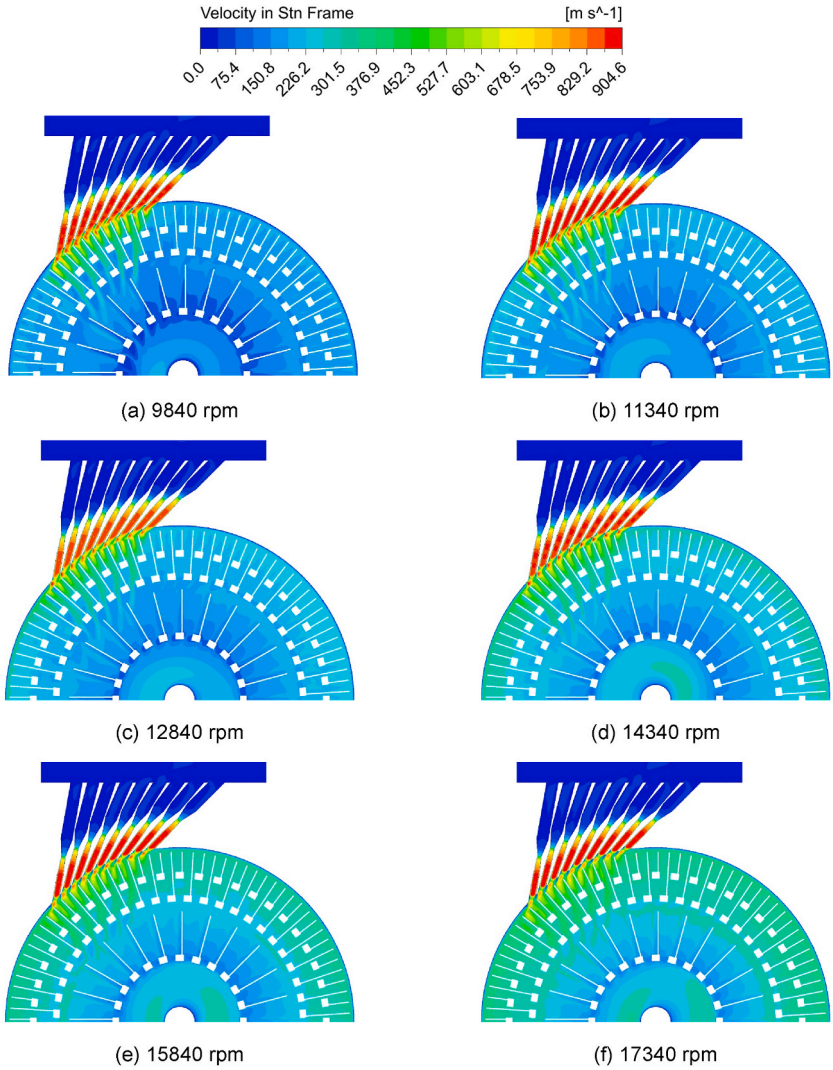

Fig. 9. Internal velocity distribution at different rotational speeds.

1500 rpm. With the increase in rotational speed, the velocity of steam inside the turbine shows a decreasing trend near the first row of bristles. Considering that torque is proportional to the square of velocity and resistance, it can be inferred that torque decreases accordingly.

Although the operating principle of the bristle turbine differs from that of conventional bladed turbines, the formation of liquid droplets should still be taken into account. The dryness field within the nozzle and rotor is depicted in Fig. 10. The minimum dryness fraction, approximately 0.88, occurs at the nozzle exit and at an intermediate position. The bristle turbine design has already considered the effects of wet steam, such as the use of erosion-resistant alloys like titanium (as utilized in experimental work [9]) to

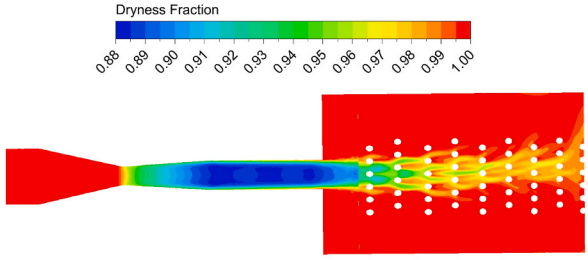

Fig. 10. Distribution of dryness inside the turbine under design conditions.

mitigate erosion and extend turbine lifespan. Therefore, a dryness fraction of 0.88 is likely acceptable for this application.

Subsequently, the static pressure and Mach number fields were analyzed, as shown in Fig. 11. At the nozzle throat, significant expansion occurred, causing a substantial drop in static pressure. As the nozzle continued to expand, the pressure gradually decreased, with the pressure at the nozzle outlet being determined by atmospheric pressure. On both the pressure and suction sides of the bristle, noticeable pressure fluctuations were observed, accompanied by shock waves. The suction side experienced a much lower pressure than the corresponding pressure on the pressure side. Additionally, the Mach number field revealed localized acceleration to supersonic speeds in certain regions, further intensifying the pressure variations and shock phenomena. As shown in Fig. 12, the trend of pressure variation along the axial direction is displayed. There is a significant pressure difference in the region where steam impacts the bristles, reaching up to 90,000 Pa under design conditions, indicating a huge load acting on the bristles to drive the turbine's rotation. As shown in Table 4, with the increase in rotational speed, the average pressure difference gradually decreases, which can prove that the load on the bristles also decreases accordingly.

In order to delve into the physical process of steam driving the rotation of the rotor, we extracted key parameters for analysis. Firstly, we calculated the drag force F_D of the bristles at different rotational speeds.

$$F_D = C_D \frac{\rho_{12} v_1^2 A_P}{2} \quad [\mathrm{N}] \tag{19}$$

A_P [m^2] represents the projected area along the jet direction, and the drag coefficient C_D is expressed as:

$$C_D = \frac{2P_{12}}{\rho_{12} v_1^2} \quad [-] \tag{20}$$

where P_{12} [Pa] represents the pressure difference between the pressure side and the suction side, ρ_{12} [$kg \cdot m^{-3}$] denotes the average steam density between both sides, and v_1 [$m \cdot s^{-1}$] stands for the average velocity on the pressure side.

In order to further compare and analyze, it is necessary to calculate the tangential force of the turbine rotor. The tangential force F_τ of the turbine rotor under different rotational speeds is expressed as:

$$F_\tau = \frac{\tau}{0.5D} \quad [\mathrm{N}] \tag{21}$$

where τ [N·m] represents the torque of the rotor. The comparison of drag and tangential forces acting on bristles at different rotational speeds is shown in Fig. 13.

From the graph, it can be observed that the trends of both forces are quite similar. The tangential force, which is deriver from torque, represents the total driving force generated by all the bristles of the turbine rotor. In contrast, the drag force only accounts for the force generated by the row of bristles primarily impacted by the steam. As a result, there is a noticeable gap between the two forces.

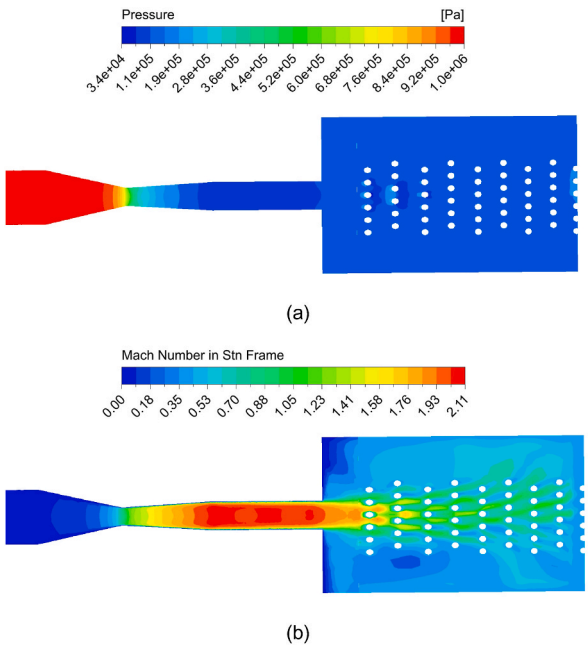

Fig. 11. Distribution of static pressure (a) and Mach number (b) inside the turbine under design conditions.

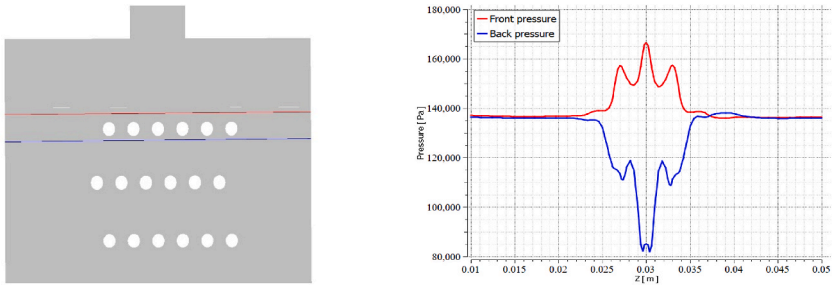

Fig. 12. Static pressure distribution along the axis.

Table 4
Average pressure difference between the pressure and suction side of bristles (0.02–0.04 m).

	Pressure side [Pa]	Suction side [Pa]	Difference [Pa]	Speed [rpm]
1	143940	123478	20462	9840
2	163027	139943	23084	11340
3	177700	161840	15860	12840
4	191230	183878	7352	14340
5	211033	205117	5916	15840
6	232439	225263	7176	17340

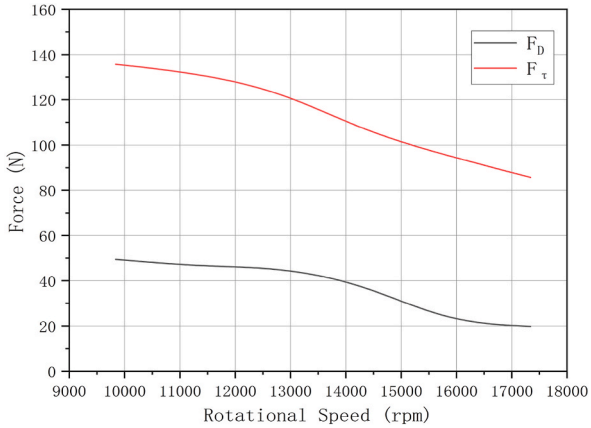

Fig. 13. Comparison of the drag force and torque-based tangential force at different speeds.

4.1.3. Energy loss analysis

By performing a quantitative analysis of various types of entropy production losses, the proportion of total energy loss can be determined. Fig. 14(a) shows the distribution of different types of entropy production losses as a function of rotational speed. From the figure, it can be observed that the entropy production losses caused by dissipation and wall effects exhibit a generally increasing trend as the rotational speed increases. In contrast, the entropy production losses caused by other factors show a decreasing trend. This behavior is due to the fact that, as rotational speed increases, the internal flow becomes more chaotic and disordered, leading to additional dissipative effects from vortices and turbulence at various scales. Simultaneously, as rotational speed increases, the difference between the steam velocity at the nozzle exit and the tangential velocity of the rotor blades gradually decreases. Consequently, shock and impact losses are reduced, leading to a corresponding decrease in losses associated with temperature changes in the medium.

Fig. 14(b) illustrates the overall proportion of the combined dissipation and wall entropy production losses for different components. As shown in the figure, the volute, which contains nine nozzles, accounts for the largest proportion of entropy production losses, reaching up to 48 % under near-optimal operating conditions (11340 rpm), whereas the outlet pipe contributes the least, with only 11 % of the entropy production losses. Under design conditions, the volute and rotor are the primary sources of energy loss. However, when deviating from the design conditions, the losses associated with the outlet pipe and cavity gaps increase, accounting for up to 43 % of the total losses at a rotational speed of 17340 rpm.

Quantitative analysis of the losses in each component alone is not sufficient to pinpoint the exact locations where energy losses occur. Dissipative effects are unavoidable in the energy conversion process, and the dissipation entropy production rate is closely

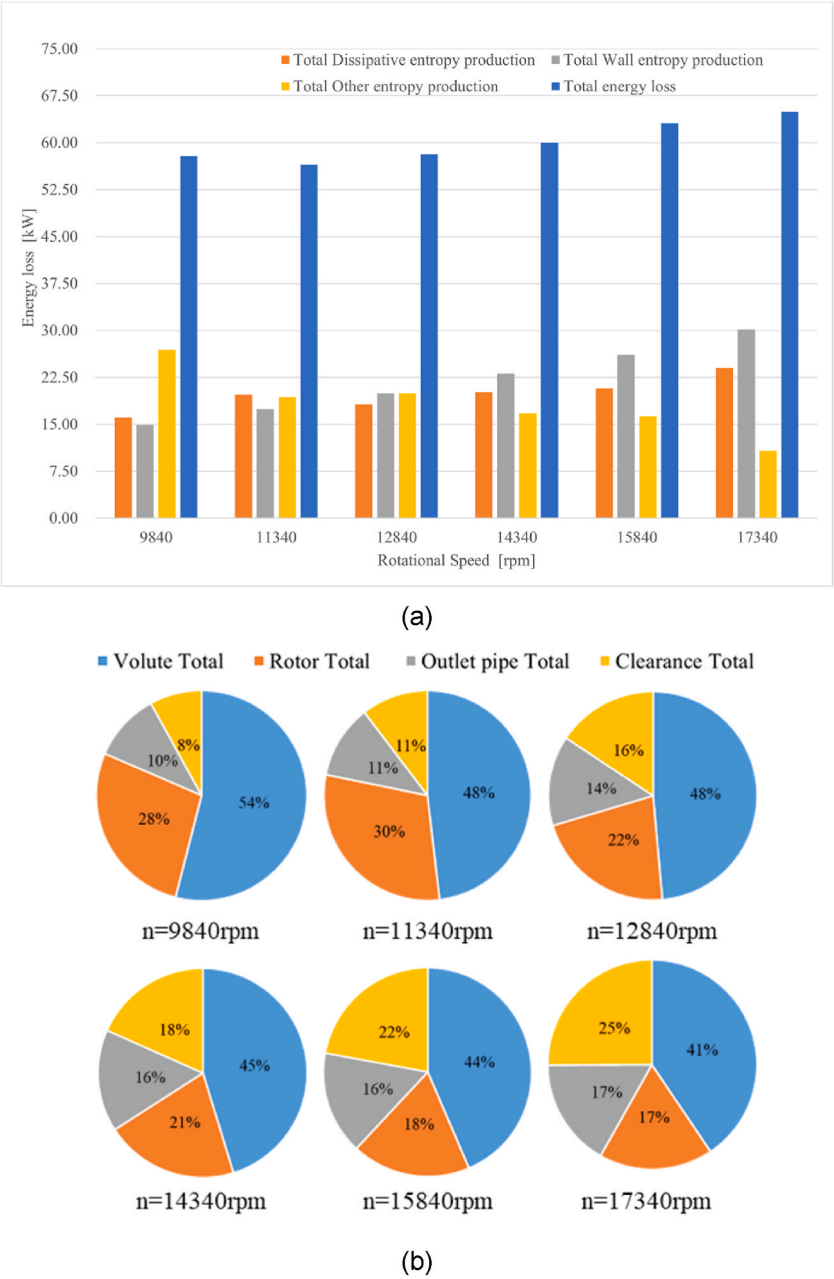

Fig. 14. Types of entropy production loss (a) and loss distribution (b) of each turbine component.

related to flow losses. By qualitatively analyzing the distribution of entropy production rates within the turbine flow passages, it is possible to identify where and how energy dissipation occurs. Fig. 15 illustrates the locations of energy dissipation within the turbine.

As steam passes through the nozzles, it is observed that the entropy increase is not significant in the converging section of the nozzles, where the velocity is relatively low. However, there are regions of higher energy dissipation in the throat and diverging sections, primarily due to wall friction losses. These losses occur near the wall surface and are caused by viscous resistance within the boundary layer. In these regions, the fluid interacts with the nozzle wall, and viscous effects lead to variations in the velocity profile, resulting in lower fluid velocity near the wall. This interaction causes energy transfer between fluid molecules, generating heat and dissipating a portion of the energy into the fluid in the form of heat. Therefore, efficient nozzle design is crucial to reducing entropy production losses caused by viscous dissipation, which is vital for improving the performance of bristle turbines.

High-velocity steam impacts the pressure surface of the bristles, creating a high-pressure region on the pressure surface, which, in turn, leads to a low-pressure region on the suction surface (as shown in Fig. 11). This pressure gradient influences the flow of the fluid. Due to the effects of inertia and the pressure gradient in high-speed flows, fluid separation occurs on the suction surface. This

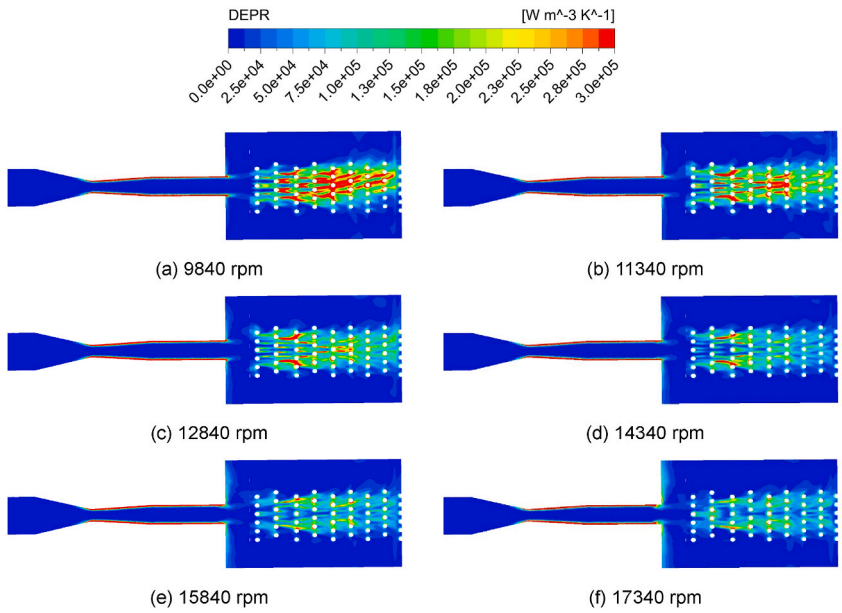

Fig. 15. Detailed distribution of internal dissipation entropy production rate (DEPR) at different speeds.

separation leads to flow instability and the formation of vortices, creating a highly turbulent dissipation region between adjacent rows of bristles. Therefore, the structure and arrangement of the bristle rotor impact elements have a significant influence on reducing turbulent dissipation.

4.2. With varying mass flow rate

When the mass flow rate or rotational speed deviates from the design values, then the turbine is running at an off-design operating point resulting in different turbine characteristics (efficiency, power output etc.). Off-design conditions occur in many occasions especially when it comes to a low-grade heat source with frequently changing parameters so turbine's flexibility is appreciated in this case.

Since a turbogenerator connected to the grid has to maintain constant frequency due to synchronization, the turbine operates at constant rotational speed even during changes to the load. In this situation, turbine power is adjusted by regulating the steam mass flow rate through a control valve located in front of the turbine. Reducing the mass flow rate affects the nozzle exit velocity and alters the flow behavior in the rotor passage.

To further validate the reliability of CFD numerical simulations, we assume that the flow regulation process is isenthalpic. When steam passes through the throttle valve, there will be changes in pressure and temperature downstream. Using REFPROP software, we calculated the downstream pressure and temperature, thereby obtaining the initial boundary conditions. Taking the uncertainty of the power analyzer used in the experiment as a reference, and based on single-sample uncertainty (as described by Moffat [27]), a uniform error of ± 0.5 kW was applied to all experimental shaft power readings. The error bands of the experiment compared with the CFD numerical simulation are shown in Fig. 16.

From the figure, it can be seen that the CFD numerical simulation results are slightly higher than the experimental ones. Excluding extreme values, the isentropic efficiency generally differs by about 5 percentage points, with the overall trend closely matching the experimental results. The CFD simulation results are based on ideal conditions with adiabatic walls specified. In practice, the steam at the turbine inlet may contain moisture or may not be fully vaporized, which is not considered in the simulation. Additionally, mechanical losses from bearings and seals are present in the experimental tests. These factors contribute to the CFD simulation results being higher than the experimental test results. Considering these factors, we can reasonably explain the deviations between the CFD simulation results and the experimental ones.

4.3. Modification of bristle geometry

The geometry of the impact elements greatly influences the aerodynamic drag generated through interaction with the working fluid, which in turn affects the torque produced by the turbine rotor. Schmirler [28] utilized a test rig with 90 kW air compressor as the source of compressed air to investigate the aerodynamic drag of impact elements with different cross-sectional shapes. The results indicated that impact elements with a square cross-section exhibited the best performance in terms of aerodynamic drag, increasing drag by 22 % compared to circular cross-sections of the same area. To verify whether the modification of the impact element would enhance the performance of the bristle turbine, the impact element shape was changed from cylindrical to square, as illustrated in

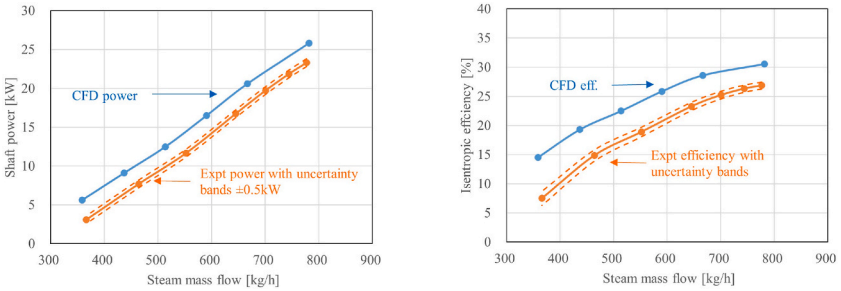

Fig. 16. Comparison of CFD numerical simulation and experimental results under different flow rates.

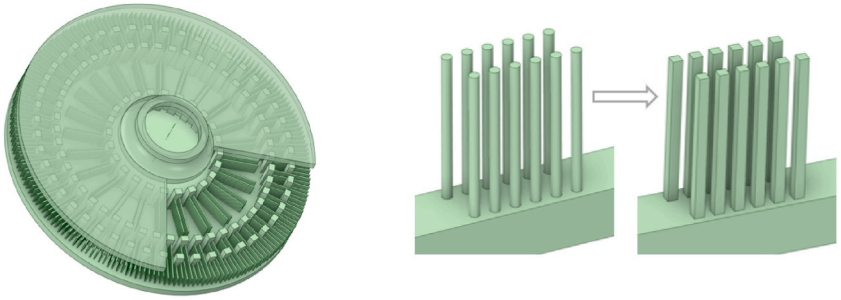

Fig. 17. Modification of rotor impact elements.

Fig. 17.

By modifying the shape of the bristles and conducting CFD numerical simulations, the differences in isentropic efficiency before and after the modification were compared, as shown in Fig. 18. The results indicate that there are no significant differences between the simulation outcomes of the two designs. This suggests that changing the impact element from a cylindrical to a square shape has a minimal effect on the performance of the bristle turbine.

Compared to the cylindrical element, the square element is more favorable for the conversion of kinetic energy. As shown in Fig. 19, when steam impacts the square element, the velocity drop per unit length is more pronounced, particularly near the edges where flow separation is more significant. The increased flow separation associated with the square design is expected to lead to higher resistance. In Fig. 20, it is evident that near the design operating conditions, the square element exhibits greater resistance when impacted by steam than the cylindrical element. The turbulence and wake region generated by the square element may introduce more flow disturbances than initially anticipated, rather than producing useful work. Excess turbulence could have dissipated energy through vortices and low-pressure regions behind the square element, negatively impacting the overall performance of the turbine. Consequently, the increase in resistance did not lead to an improvement in the performance of the bristle turbine. This analysis highlights the importance of optimizing element shapes and configurations to balance the benefits of kinetic energy conversion against potential increases in drag and flow disturbances. Further design refinements may be necessary to enhance the efficiency of the bristle turbine.

4.4. Discussion

Conventional turbines, even in small-scale applications, benefit from decades of optimization and design refinement. The aerodynamics, blade geometry, materials, and operating conditions of traditional turbines have been thoroughly studied and adjusted to

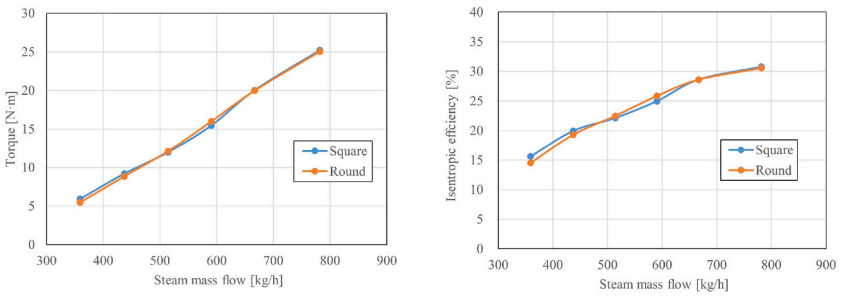

Fig. 18. Differences between impact elements of different shapes.

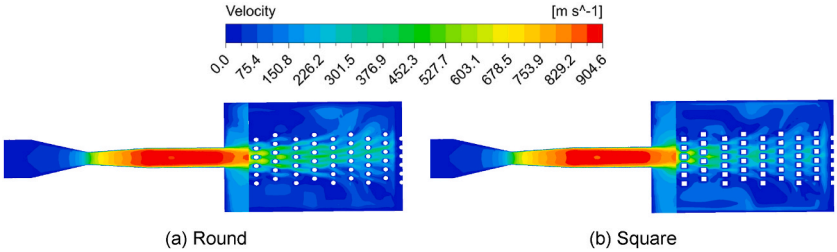

Fig. 19. The velocity distribution of different impact elements.

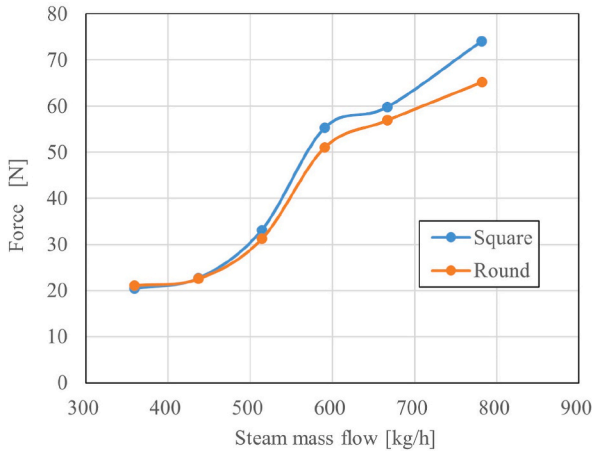

Fig. 20. Differences in drag forces of different impact elements.

maximize efficiency, often exceeding 50 % even in smaller models. In contrast, the bristle turbine is a relatively new and less explored design, with maximum efficiencies in existing reports still below 35 %, indicating significant optimization potential yet to be realized.

In conventional turbines, blades are engineered to convert fluid energy efficiently due to their highly aerodynamic shapes, which minimize losses from turbulence and friction. The working principle of a bristle turbine, however, is quite different. Energy transfer relies on interactions between the fluid and the bristle elements, which may lead to greater energy dissipation due to increased turbulence, friction, and wake formation compared to smooth aerodynamic blades. Moreover, the more complex interaction between the bristles and the steam can result in higher mechanical losses. In the future, we will take this as an opportunity to further explore hog bristle turbines, aiming to achieve optimal bristle shapes and arrangements that maintain the benefits of turbulence enhancement while minimizing unnecessary energy losses.

Additionally, conventional impulse turbines feature carefully optimized nozzle designs that ensure the fluid impacts the blades at the most efficient angles. This aspect presents an opportunity for further refinement in our bristle turbine design.

5. Conclusions and recommendations

(1) This study conducted CFD numerical simulations of the bristle turbine, verifying the feasibility of applying CFD to bristle turbines. The results demonstrated a high level of agreement between CFD simulations and experimental tests, with a relative error of around 10 %, indicating a certain degree of accuracy.

(2) Under constant expansion ratio and mass flow rate conditions, the turbine performance under off-design conditions was predicted by varying the rotational speed of the rotating domain. The results showed that the design point is not the optimal operating condition, with the highest efficiency occurring at a speed ratio of approximately 0.27. Therefore, selecting an appropriate rotational speed can further improve the performance of the bristle turbine.

(3) By establishing a profile of a single nozzle and calculating the drag force exerted on the bristles near the nozzle outlet based on the pressure difference across the first row of bristles, it was found that the drag force on the bristles is consistent with the trend of the tangential force provided by the turbine torque as the rotational speed changes. This reveals the aerodynamic characteristics within the turbine, filling a gap in the research on internal flow in bristle turbines.

(4) Using entropy production theory, the energy loss proportion of each component of the bristle turbine was analyzed. The results indicate that the volute and rotor are the primary components contributing to energy loss. Further optimization of the nozzle and rotor bristles can be used to enhance the performance of the bristle turbine.

(5) The turbine configuration was altered by modifying the shape of the bristles in the bristle turbine. It was found that replacing cylindrical short rods with square short rods did not significantly improve performance, indirectly suggesting that the choice of bristle shape in the manufacturing process can be made based on budget constraints.

CRediT authorship contribution statement

Sun Sheng Yang: Writing – original draft. **Dong Ya Li:** Writing – original draft, Methodology. **David Kupka:** Writing – review & editing, Funding acquisition. **Jan Kolonicny:** Writing – review & editing, Data curation. **Punit Singh:** Writing – review & editing, Supervision.

Declaration of competing interest

The authors declare that they have no known competing financial interests or personal relationships that could have appeared to influence the work reported in this paper.

Acknowledgments

This work was supported by the National Natural Science Foundation of China (Grant No. 52079058). And the computational resource was supported by Jiangsu University and Indian Institute of Science. This work was also supported by the Technology Agency of the Czech Republic, project TN02000025 National Centre for Energy II. In addition, the authors wish to express special thanks to Ferdinand Madry for his assistance and input throughout the development of the bristle turbine.

Data availability

Data will be made available on request.

References

[1] H. Jouhara, N. Khordehgah, S. Almahmoud, B. Delpech, A. Chauhan, S.A. Tassou, Waste heat recovery technologies and applications, Therm. Sci. Eng. Prog. 6 (2018) 268–289, https://doi.org/10.1016/j.tsep.2018.04.017.
[2] Z. Su, M. Zhang, P. Xu, Z. Zhao, Z. Wang, H. Huang, T. Ouyang, Opportunities and strategies for multigrade waste heat utilization in various industries: a recent review, Energy Convers. Manag. 229 (2021) 113769, https://doi.org/10.1016/j.enconman.2020.113769.
[3] J. Qian, L. Wei, M. Zhang, F. Chen, L. Chen, W. Jiang, Z. Jin, Flow rate analysis of compressible superheated steam through pressure reducing valves, Energy 135 (2017) 650–658, https://doi.org/10.1016/j.energy.2017.06.170.
[4] G.F. Frate, L. Ferrari, R. Lensi, U. Desideri, Steam expander as a throttling valve replacement in industrial plants: a techno-economic feasibility analysis, Appl. Energy 238 (2019) 11–21, https://doi.org/10.1016/j.apenergy.2019.01.005.
[5] S.O. Oyedepo, B.A. Fakeye, Waste heat recovery technologies: pathway to sustainable energy development, J. Therm. Eng. 7 (2021) 324–348, https://doi.org/10.18186/thermal.850796.
[6] N. Peng, E. Wang, W. Wang, Design and analysis of a 1.5 kW single-stage partial-admission impulse turbine for low-grade energy utilization, Energy 268 (2023) 126631, https://doi.org/10.1016/j.energy.2023.126631.
[7] N. Peng, E. Wang, W. Wang, J. Lu, M. Li, Aerodynamic analysis of a 1.5 kW two-stage counter-rotating partial-admission impulse turbine for small-scale power system with a high expansion pressure ratio, Case Stud. Therm. Eng. 53 (2024) 103824, https://doi.org/10.1016/j.csite.2023.103824.
[8] N. Peng, E. Wang, F. Meng, W. Zhang, Y. Wang, B. Zhang, E.C. Yenga Yenga, Experimental investigation on off-design performance of a small-scale two-stage counter-rotating impulse turbine, Int. J. Energy Res. 2024 (1) (2024) 4623244, https://doi.org/10.1155/2024/4623244.
[9] D. Kupka, J. Koloničný, Design and experimental investigation of a micro-scale bladeless-type steam turbine, Appl. Therm. Eng. 239 (2024) 122119, https://doi.org/10.1016/j.applthermaleng.2023.122119.
[10] C.K. Kim, J.Y. Yoon, Performance analysis of bladeless jet propulsion micro-steam turbine for micro-CHP (combined heat and power) systems utilizing low-grade heat sources, Energy 101 (2016) 411–420, https://doi.org/10.1016/j.energy.2016.01.070.
[11] S. Barbarelli, G. Florio, N. Scornaienchi, Theoretical and experimental analysis of a new compressible flow small power turbine prototype, Int. J. Heat Technol. 35 (2017) S391–S398, https://doi.org/10.18280/ijht.35Sp0153.
[12] A. Ganguly, S. Sengupta, S. Pramanik, Waste heat recovery using Tesla turbines in Rankine cycle power plants: thermofluid dynamic characterization, performance assessment and exergy analysis, Appl. Therm. Eng. 207 (2022) 118141, https://doi.org/10.1016/j.applthermaleng.2022.118141.
[13] M.S. Siddiqui, H. Ahmed, S. Ahmed, Numerical simulation of a compressed air driven Tesla turbine, in: ASME 2014 Power Conference, American Society of Mechanical Engineers, 2014, https://doi.org/10.1115/POWER2014-32069.
[14] S. Akele, M.O. Ahmed, S.J. Wodah, J. Agbajor, K.O. Ihwurighwre, O. Uwumagbuhun, O. Uwumagbuhun, O. Uwumagbuhun, Design and CFD simulation of Tesla pump, Int. J. Eng. Manag. Res. 11 (2021), https://doi.org/10.31033/ijemr.11.3.7.
[15] L. Ciappi, D. Fiaschi, P.H. Niknam, L. Talluri, Computational investigation of the flow inside a Tesla turbine rotor, Energy 173 (2019) 207–217, https://doi.org/10.1016/j.energy.2019.01.158.
[16] C. Schosser, S. Lecheler, M. Pfitzner, Analytical and numerical solutions of the rotor flow in Tesla turbines, Period. Polytech. - Mech. Eng. 61 (2017) 12–22, https://doi.org/10.3311/PPme.9000.
[17] G. Manfrida, L. Talluri, Fluid dynamics assessment of the Tesla turbine rotor, Therm. Sci. 23 (2019) 1–10, https://doi.org/10.2298/TSCI160601170M.
[18] Hamdani Umar, Teuku Muhammad Kashogi, Sarwo Edhy Sofyan, Razali Thaib, Akram, CFD simulation of Tesla turbines performance driven by flue gas of internal combustion engine, J. Adv. Res. App. Mechan. 98 (2022) 1–11, https://doi.org/10.37934/aram.98.1.111.
[19] E. Benini, S. Giacometti, Design, manufacturing and operation of a small turbojet-engine for research purposes, Appl. Energy 84 (2007) 1102–1116, https://doi.org/10.1016/j.apenergy.2007.05.006.
[20] S. Barbarelli, G. Florio, N.M. Scornaienchi, Performance analysis of a low-power tangential flow turbine with rotary channel, J. Energy Resour. Technol. 127 (2005) 272–279, https://doi.org/10.1115/1.1944008.
[21] N.M. Scornaienchi, G. Florio, M.A. Belli, Small power turbine characterized by a tangential flow within a rotary channel, in: ESDA 94 Proc. Of Second Biennal European Conf. on Engineering System and Analysis, ASME, New York, 1994, pp. 511–551.
[22] S. Barbarelli, G. Florio, N.M. Scornaienchi, Developing of a small power turbine recovering energy from low enthalpy steams or waste gases: design, building and experimental measurements, Therm. Sci. Eng. Prog. 6 (2018) 346–354, https://doi.org/10.1016/j.tsep.2017.12.007.

[23] O.E. Balje, Turbomachines: A Guide to Design Selection and Theory, Wiley, New York, 1981.
[24] E.W. Lemmon, M.L. Huber, M.O. McLinden, NIST standard reference database 23. Reference Fluid Thermodynamic and Transport Properties (REFPROP), version, 2010, p. 9.
[25] F. Kock, H. Herwig, Local entropy production in turbulent shear flows: a high-Reynolds number model with wall functions, Int. J. Heat Mass Tran. 47 (2004) 2205–2215, https://doi.org/10.1016/j.ijheatmasstransfer.2003.11.025.
[26] L. Duan, X. Wu, Z. Ji, Z. Xiong, J. Zhuang, The flow pattern and entropy generation in an axial inlet cyclone with reflux cone and gaps in the vortex finder, Powder Technol. 303 (2016) 192–202, https://doi.org/10.1016/j.powtec.2016.09.019.
[27] R.J. Moffat, Contributions to the theory of single-sample uncertainty analysis. https://doi.org/10.1115/1.3241818, 1982.
[28] M. Schmirler, The brush turbine unit with an axial ram elements, AIP Conf. Proc. 1768 (2016) 020009, https://doi.org/10.1063/1.4963031.

Nomenclature

Symbols

A: area (m^2)
c_{pm}*:* specific heat capacity at constant pressure (J/kgK)
d: diameter (m)
h: specific enthalpy (J/kg)
k: turbulence kinetic energy (J/kg)
n: rotational speed (rpm)
p: pressure (Pa)
P: power (W)
S: entropy production rate (W/m^3K)
t: time (s)
T: temperature (K)
u, v, w: velocity components (m/s)
V: volume (m^3)
x, y, z: directions of the Cartesian coordinates
ϵ*:* turbulent dissipation rate (m^2/s^3)
κ*:* specific heat ratio (−)
μ*:* dynamic viscosity (Pa·s)
ρ*:* density (kg/m^3)
τ*:* torque (N·m), wall shear stress (Pa)
ψ*:* stage loading coefficient (−)
Φ*:* flow coefficient (−)

Abbreviations

CD –: convergent-divergent nozzle
CFD –: computational fluid dynamics
DEPR –: dissipation entropy production rate
Ds –: specific diameter
EES –: engineering equation solver
EPR –: entropy production rate
GGI –: general grid interface
PR –: pressure ratio
RANS –: Reynolds-Averaged Navier-Stokes
Ns –: specific speed